Extraction-controlled terahertz frequency quantum cascade lasers with a diagonal LO-phonon extraction and injection stage

Y. J. Han,[1,*] L. H. Li,[1] A. Grier,[1] L. Chen,[1] A. Valavanis,[1] J. Zhu,[1] J. R. Freeman,[1] N. Isac,[2] R. Colombelli,[2] P. Dean,[1] A. G. Davies,[1] and E. H. Linfield[1]

[1]*School of Electronic and Electrical Engineering, University of Leeds, Leeds LS2 9JT, UK*
[2]*Centre for Nanoscience and Nanotechnology (C2N Orsay), CNRS UMR9001, Univ. Paris Sud, Univ. Paris Saclay, 91405 Orsay, France*
[*]*y.han@leeds.ac.uk*

Abstract: We report an extraction-controlled terahertz (THz)-frequency quantum cascade laser design in which a diagonal LO-phonon scattering process is used to achieve efficient current injection into the upper laser level of each period and simultaneously extract electrons from the adjacent period. The effects of the diagonality of the radiative transition are investigated, and a design with a scaled oscillator strength of 0.45 is shown experimentally to provide the highest temperature performance. A 3.3 THz device processed into a double-metal waveguide configuration operated up to 123 K in pulsed mode, with a threshold current density of 1.3 kA/cm^2 at 10 K. The QCL structures are modeled using an extended density matrix approach, and the large threshold current is attributed to parasitic current paths associated with the upper laser levels. The simplicity of this design makes it an ideal platform to investigate the scattering injection process.

References and links

1. R. Köhler, A. Tredicucci, F. Beltram, H. E. Beere, E. H. Linfield, A. G. Davies, D. A. Ritchie, R. C. Iotti, and F. Rossi, "Terahertz semiconductor-heterostructure laser," Nature **417**, 156–159 (2002).
2. B. S. Williams, "Terahertz quantum-cascade lasers," Nature Photonics **1**, 517–525 (2007).
3. G. Scalari, C. Walther, M. Fischer, R. Terazzi, H. Beere, D. Ritchie, and J. Faist, "Thz and sub-thz quantum cascade lasers," Laser & Photonics Reviews **3**, 45–66 (2009).
4. S. Kumar, "Recent progress in terahertz quantum cascade lasers," IEEE J. Sel. Top. Quant. **17**, 38–47 (2011).
5. M. Wienold, B. Röben, L. Schrottke, R. Sharma, A. Tahraoui, K. Biermann, and H. T. Grahn, "High-temperature, continuous-wave operation of terahertz quantum-cascade lasers with metal-metal waveguides and third-order distributed feedback," Opt. Express **22**, 3334–3348 (2014).
6. C. Walther, M. Fischer, G. Scalari, R. Terazzi, N. Hoyler, and J. Faist, "Quantum cascade lasers operating from 1.2 to 1.6 Thz," Appl. Phys. Lett. **91**, 131122 (2007).
7. C. W. Chan, Q. Hu, and J. L. Reno, "Ground state terahertz quantum cascade lasers," Appl. Phys. Lett. **101**, 151108 (2012).
8. L. Li, L. Chen, J. Zhu, J. Freeman, P. Dean, A. Valavanis, A. G. Davies, and E. H. Linfield, "Terahertz quantum cascade lasers with >1 W output powers," Electron. Lett. **50**, 309–311 (2014).
9. M. Tonouchi, "Cutting-edge terahertz technology," Nature Photonics **1**, 97–105 (2007).
10. P. Dean, A. Valavanis, J. Keeley, K. Bertling, Y. L. Lim, R. Alhathlool, A. D. Burnett, L. H. Li, S. P. Khanna, D. Indjin, T. Taimre, A. D. Rakić, E. H. Linfield, and A. G. Davies, "Terahertz imaging using quantum cascade lasers - review of systems and applications," J. Phys. D **47**, 374008 (2014).
11. S. Fathololoumi, E. Dupont, C. W. I. Chan, Z. R. Wasilewski, S. R. Laframboise, D. Ban, A. Mátyás, C. Jirauschek, Q. Hu, and H. C. Liu, "Terahertz quantum cascade lasers operating up to ∼ 200 K with optimized oscillator strength and improved injection tunneling," Opt. Express **20**, 3866 (2012).
12. D. Indjin, P. Harrison, R. W. Kelsall, and Z. Ikonić, "Mechanisms of temperature performance degradation in terahertz quantum-cascade lasers," Appl. Phys. Lett. **82**, 1347–1349 (2003).
13. Y. J. Han and J. C. Cao, "Monte carlo simulation of carrier dynamics in terahertz quantum cascade lasers," J. Appl. Phys. **108**, 093111 (2010).

14. Y. Chassagneux, Q. J. Wang, S. P. Khanna, E. Strupiechonski, J. R. Coudevylle, E. H. Linfield, A. G. Davies, F. Capasso, M. A. Belkin, and R. Colombelli, "Limiting factors to the temperature performance of thz quantum cascade lasers based on the resonant-phonon depopulation scheme," IEEE Transactions on THz Science and Technology **2**, 83–92 (2012).

15. S. Kumar, Q. Hu, and J. L. Reno, "186 K operation of terahertz quantum-cascade lasers based on a diagonal design," Appl. Phys. Lett. **94**, 131105 (2009).

16. S. Fathololoumi, E. Dupont, Z. R. Wasilewski, C. W. Chan, S. G. Razavipour, S. R. Laframboise, S. X. Huang, Q. Hu, D. Ban, and H. C. Liu, "Effect of oscillator strength and intermediate resonance on the performance of resonant phonon-based terahertz quantum cascade lasers," J. Appl. Phys. **113**, 113109 (2013).

17. H. Yasuda, T. Kubis, P. Vogl, N. Sekine, I. Hosako, and K. Hirakawa, "Nonequilibrium Green's function calculation for four-level scheme terahertz quantum cascade lasers," Appl. Phys. Lett. **94**, 151109 (2009).

18. T. Liu, T. Kubis, Q. J. Wang, and G. Klimeck, "Design of three-well indirect pumping terahertz quantum cascade lasers for high optical gain based on nonequilibrium Green's function analysis," Appl. Phys. Lett. **100**, 122110 (2012).

19. S. Kumar, C. W. Chan, Q. Hu, and J. L. Reno, "A 1.8-Thz quantum cascade laser operating significantly above the temperature of $\hbar\omega/k_B$," Nature Physics **7**, 166–171 (2011).

20. E. Dupont, S. Fathololoumi, Z. R. Wasilewski, G. Aers, S. R. Laframboise, M. Lindskog, S. G. Razavipour, A. Wacker, D. Ban, and H. C. Liu, "A phonon scattering assisted injection and extraction based terahertz quantum cascade laser," J. Appl. Phys. **111**, 073111 (2012).

21. K. Fujita, M. Yamanishi, S. Furuta, K. Tanaka, T. Edamura, T. Kubis, and G. Klimeck, "Indirectly pumped 3.7 Thz InGaAs/InAlAs quantum-cascade lasers grown by metal-organic vapor-phase epitaxy," Opt. Express **20**, 20647 (2012).

22. S. G. Razavipour, E. Dupont, C. W. Chan, C. Xu, Z. R. Wasilewski, S. R. Laframboise, Q. Hu, and D. Ban, "A high carrier injection terahertz quantum cascade laser based on indirectly pumped scheme," Appl. Phys. Lett. **104**, 041111 (2014).

23. A. Wacker, "Extraction-controlled quantum cascade lasers," Appl. Phys. Lett. **97**, 081105 (2010).

24. B. S. Williams, S. Kumar, H. Callebaut, Q. Hu, and J. L. Reno, "Terahertz quantum-cascade laser at lambda approximate to 100 μm using metal waveguide for mode confinement," Appl. Phys. Lett. **83**, 2124–2126 (2003).

25. A. Albo and Q. Hu, "Carrier leakage into the continuum in diagonal GaAs/Al$_{0.15}$GaAs terahertz quantum cascade lasers," Appl. Phys. Lett. **107**, 241101 (2015).

26. A. Albo, Q. Hu, and J. L. Reno, "Room temperature negative differential resistance in terahertz quantum cascade laser structures," Appl. Phys. Lett. **109**, 081102 (2016).

27. T. V. Dinh, A. Valavanis, L. J. M. Lever, Z. Ikonic, and R. W. Kelsall, "Extended density-matrix model applied to silicon-based terahertz quantum cascade lasers," Phys. Rev. B **85**, 235427 (2012).

28. R. Terazzi, T. Gresch, A. Wittmann, and J. Faist, "Sequential resonant tunneling in quantum cascade lasers," Phys. Rev. B **78**, 155328 (2008).

29. A. Grier, "Modelling the optical and electronic transport properties of AlGaAs and AlGaN intersubband devices and optimisation of quantum cascade laser active regions," PhD thesis, **Chapter 4** (Univ. of Leeds, 2015).

30. E. Dupont, S. Fathololoumi, and H. C. Liu, "Simplified density-matrix model applied to three-well terahertz quantum cascade lasers," Phys. Rev. B **81**, 205311 (2010).

31. C. W. I. Chan, "Towards room-temperature Thz QCLs : directions and design," PhD thesis, **Chapter 6** (Massachusetts Institute of Technology, Department of Electrical Engineering and Computer Science, 2015).

32. M. Francki, D. O. Winge, J. Wolf, V. Liverini, E. Dupont, V. Trinit, J. Faist, and A. Wacker, "Impact of interface roughness distributions on the operation of quantum cascade lasers," Opt. Express **23**, 5201–5212 (2015).

1. Introduction

Terahertz-frequency quantum cascade lasers (THz QCLs) have undergone steady development since their first demonstration in 2002 [1–5]. To date, their emission frequency has covered the range from 1.2 THz to 5.2 THz [6, 7], and the maximum peak output power has reached 1.01 W in pulsed mode at 10 K [8]. These improvements now establish THz QCLs as promising sources for many applications including THz spectroscopy, remote sensing and THz imaging [9, 10]. However, the maximum operating temperature of THz QCLs to date is only 199.5 K [11], which limits their practical use in many applications outside the laboratory environment. Improving the performance of THz QCLs at higher temperatures is therefore of critical importance.

One of the main mechanisms attributed to the degradation of THz QCL performance with increasing temperature is thermally activated longitudinal-optic (LO)-phonon scattering between laser levels, which leads to a rapid loss of the population in the upper laser state at high temperatures [12–14]. One solution to improve the performance at higher temperatures is to suppress phonon scattering between the laser levels by using designs based on a diagonal
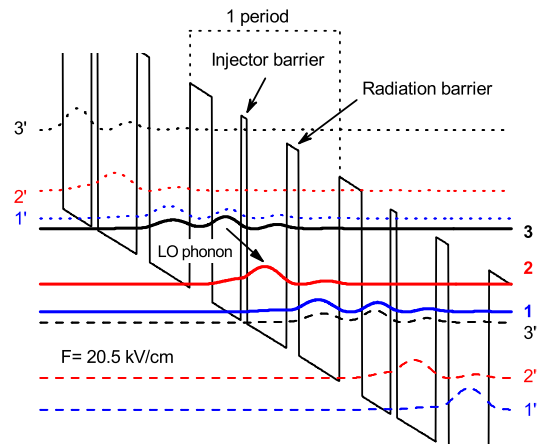
Fig. 1. Calculated conduction band diagram and squared moduli of the electronic wave functions of a three-level design (D2) in GaAs/Al$_{0.15}$Ga$_{0.85}$As at an electric field of 20.5 kV/cm. Subbands 2 and 1 are the laser levels, and the carriers are injected from subband 3 to 2 by LO-phonon scattering. The layer sequence of an active module and the design parameters are listed in Table 1.

radiative transition [11, 15, 16]. Alternatively, an indirect injection scheme [17–22] can be used, in which LO-phonon scattering replaces resonant tunneling for carrier injection; QCL devices based on this indirect injection scheme have operated up to 163 K at 1.8 THz [19]. A simple 'extraction-controlled' design has also been proposed [23], in which only one phonon scattering process is employed to realize both carrier extraction and injection simultaneously; this contrasts with the two LO-phonon scattering processes used for separate carrier extraction and injection in previous indirect injection schemes. Here, we present a new extraction-controlled design in which a diagonal LO-phonon extraction and injection stage is used to increase the carrier injection efficiency. Our design has only three subbands within each module, and its simplicity makes it an ideal platform to investigate the scattering injection process for high temperature operation of THz QCLs.

2. Active region design

The conduction band profile and the squared moduli of the electronic wavefunctions of three periods of our GaAs/Al$_{0.15}$Ga$_{0.85}$As structure at the design bias are shown in Fig. 1. The ground states in three adjacent quantum wells are used to achieve the scattering injected design. Levels 2 and 1 are the laser states for the emission of THz radiation; level 3 behaves simultaneously as the injector level of the same period and as the extractor level of the previous period. The energy separation between levels 3 and 2 is designed to be equal to the LO-phonon energy, enabling fast resonant LO-phonon scattering from level 3 to level 2. Owing to the strong coupling between level 1 and level 3″ (the injection level of the next period), the electrons in level 1 are extracted rapidly via resonant tunneling and subsequently by LO phonon scattering. This leads to a short lifetime for level 1, and hence a population inversion between laser levels 2 and 1. The LO-phonon extraction/injection transition is spatially diagonal, with the carriers being transported between two wells, separated by a thin injector barrier. The purpose of this is to increase the carrier injection selectivity, and at the same time to maintain the strong LO phonon scattering between level 3 and level 2. The lower laser level 1 is confined in the third quantum well to make the radiative transition also diagonal in space, which helps to reduce the carrier leakage from the upper laser level 2 to the lower levels. This diagonality is determined mainly

Table 1. Overview of the layer sequences and key parameters of the four designs. The layer thicknesses of one active module are given with the $Al_{0.15}Ga_{0.85}As$ barriers in bold and GaAs wells in plain text. The underlined wells are doped with Si at the level of 2.66×10^{16} cm^{-3}, 2.61×10^{16} cm^{-3}, 2.62×10^{16} cm^{-3} and 2.58×10^{16} cm^{-3} for D1 − D4 respectively, yielding average bulk level of 5.0×10^{15} cm^{-3} per period. $E_3 - E_2$ is the energy separation between subbands 3 and 2, $E_2 - E_1$ is the energy separation between subbands 2 and 1, f_{21} is the scaled oscillator strength, and $\Delta_{1'3}$ is the anticrossing gap energy of the subbands $1'$ and 3. The principal difference between the four designs is the optical transition diagonality, which is characterized by f_{21}.

Active region design	Thickness (nm)	$E_3 - E_2$ (meV)	$E_2 - E_1$ (meV)	f_{21} (a.u.)	$\Delta_{1'3}$ (meV)
D1	**4.4**/<u>5.6</u>/**1.2**/7.7/**2.8**/8.1	34.8	16.3	0.32	6.7
D2	**4.4**/<u>5.6</u>/**1.2**/7.7/**2.4**/7.9	34.7	16.5	0.45	6.6
D3	**4.2**/<u>5.5</u>/**1.2**/8.1/**2.0**/7.8	34.6	16.4	0.62	6.7
D4	**4.0**/<u>5.5</u>/**1.2**/8.5/**1.7**/7.5	34.3	16.3	0.82	6.9

by the thickness of the radiation barrier, which separates the laser levels 2 and 1 into different quantum wells. As summarised in Table 1, four structures have been investigated with different degrees of optical transition diagonality.

3. Experiment results

The samples were grown on semi-insulating GaAs substrates by molecular beam epitaxy. A 300-nm-thick $Al_{0.55}Ga_{0.45}As$ layer was first grown as an etch stop layer for use in the metal-metal waveguide fabrication. Each QCL structure consisted of a 10-μm-thick periodic stack (consisting of 336, 343, 348, and 353 periods for D1 − D4, respectively) of the three-well active modules, embedded between two n$^+$-GaAs layers. The lower GaAs layer was 100 nm thick and the upper GaAs layer was 50 nm thick. Both layers were Si doped at a level of n = 5.0×10^{18} cm^{-3}. Following growth, the QCL wafers were thermo-compression bonded to n$^+$-GaAs acceptor wafers, and devices were fabricated using a gold-gold waveguide configuration [24]. After removal of the growth substrate, a non-alloyed Ti/Au (10/150 nm) layer was deposited as the top waveguide layer and the laser ridges were etched in a $H_2SO_4 : H_2O_2 : H_2O$ (1:8:1) solution. After substrate thinning to a thickness of 180 μm, and back-side metallization, laser bars were cleaved and indium-soldered to copper submounts. For the light power-current-voltage (*L-I-V*) and spectral characterization, the devices were operated in pulsed mode with 2-μs-long pulses at a repetition rate of 10 kHz and the laser emission was detected using a cooled Ge:Ga photoconductive detector. In order to match the detector response time, the pulse train was gated with a slow 167 Hz modulation with 50% duty cycle. The output power was calibrated separately with an absolute THz power meter (Thomas-Keating Instruments) using a gate frequency of 30 Hz.

Figure 2(a) shows the *L-I-V* curves measured for design D2, for which $f_{21} = 0.45$. The device lased up to 123 K in pulsed mode, which is the maximum operating temperature of the four designs. At a temperature of 10 K, the threshold current density (J_{th}) was 1.29 kA/cm^2, the peak output power was 4.8 mW at a current density of 1.60 kA/cm^2, and the slope efficiency was 14 mW/A. The peak power is comparable with other indirect injection designs [20-22], but the current is much higher, resulting in significant Joule heating within the device. A regression of the temperature evolution of the threshold current density to the empirical equation $J_{th} = J_0 + J_1 exp(T/T_0)$ yields the value $T_0 = 27$ K. The small T_0 indicates large thermally activated current, resulting in a large threshold current density of 1.58 kA/cm^2 at 123 K. The emission spectra measured at a range of biases are shown in Fig. 2(b). The emission frequency was centered at ∼ 3.1 THz at biases close to threshold, and a heat-sink temperature of 10 K.
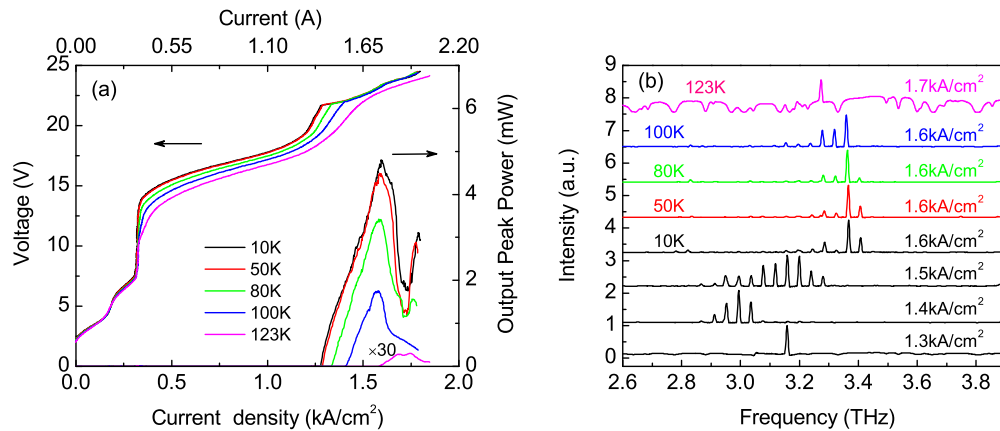
Fig. 2. (a) Output power-current density-applied voltage (*L-I-V*) characteristics of design D2 at various temperatures. (b) Spectra at various current densities and temperatures. The device was 1000 μm long and 110 μm wide, processed into a gold-gold waveguide configuration, and operated in pulsed mode with 2-μs-long pulses at a repetition rate of 10 kHz.

With increasing bias, the spectra broadened and multi-mode lasing behavior was observed over the range 2.9 to 3.4 THz. When the temperature increased to 123 K, only the mode at 3.3 THz remained. The *I-V* curve at 10 K exhibits three distinct step increases in the current density before the threshold current is reached; the first increase to 0.20 kA/cm^2, the second to 0.32 kA/cm^2 and the third to 1.20 kA/cm^2, with corresponding applied voltages roughly coincident with those for the alignment of the subbands 1−1″, 1−2″ and 2−3″, respectively. These three increases of current are indicative of parasitic paths for the carrier transport, which might be related to the resonant coupling of the subbands described above. At elevated temperatures, the onset bias of the third current step decreases to 10.2 V, indicating thermal activation of the parasitic path.

The device performance is dependent on the diagonality of the optical transition. Four designs (D1 − D4) with f_{21} varying from 0.32 to 0.82 were investigated, and the *I-V* curves and emission spectra measured at 10 K are compared in Fig. 3. As shown in Fig. 3(b), similar lasing frequencies at the design bias indicate good control over the material growth. The differences in the *I-V* curves and the maximum operating temperatures can, therefore, be attributed principally to the difference in the oscillator strength f_{21}. The key features of the *I-V* curves are the same in each case, i.e., three distinct step increases in current are separated by regions of negative differential resistance (NDR) before the threshold is reached. The main difference between the *I-V* curves is the marked increase in current for designs with large oscillator strength f_{21}, especially for the last two current steps. With the increase of f_{21} (D1 − D4), the current density rises to 0.22 kA/cm^2 (D1) and 0.53 kA/cm^2 (D4) in the second step, and to 1.0 kA/cm^2 (D1) and 2.0 kA/cm^2 (D4) in the third step, indicating the enhanced effects of these two parasitic paths. It is also noted that in each case there is no observable NDR region after the lasing range, which is normally observed in three-well resonant phonon designs [11]. This indicates that the current keeps flowing after the alignment of the subbands 1−3″ is broken. Considering the applied voltages are quite high, it is possible the carriers could leak into the higher states or continuum states [25, 26], which could be another reason for the high current and the low operating temperatures. The effects of the oscillator strength on the maximum operating temperature are shown in the inset of Fig. 3(a). Due to the trade-off between oscillator strength and population inversion, an optimum value of oscillator strength was found to be around $f_{21} = 0.4 − 0.5$.
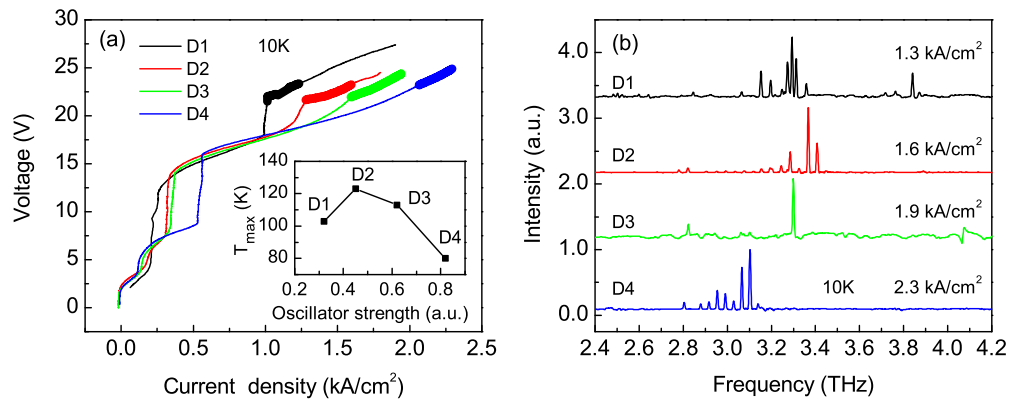
Fig. 3. (a) *I-V* characteristics of the four designs at 10 K. The regions of the *I-V* curves shown in thicker lines indicate the lasing ranges. Inset: the maximum operating temperatures. (b) Spectra of the four designs at 10 K, measured at the conditions of maximum output power for each. All devices were processed into a gold-gold waveguide configuration, and operated with 2-μs-long voltage pulses at a repetition rate of 10 kHz.

4. Numerical results

To analyze the parasitic paths and the temperature performance degradation, an extended density matrix (DM) approach was used to simulate the carrier transport [27]. This approach is capable of modelling QCLs with an arbitrary number of subbands, and there is no need to manually designate an injector subband in advance. The subband wavefunctions for one period were calculated based on a tight-binding model, in which a period of the QCL structure is embedded between thick layers of the barrier material. These localized wavefunctions were also shifted along the growth direction to upstream and downstream periods, and three neighboring periods were selected in our DM approach. The assumption was made that carrier transport is determined only by interperiod resonant tunneling and intraperiod scattering. The coherence coupling of the subbands in the neighboring period was described by Rabi oscillations, with energy $\hbar\Omega$, across the barrier separating the periods. This coherence coupling is closely related with the resonant tunneling time. The intraperiod transport was computed by Monte Carlo model [13] including phonon scattering, electron-electron scattering, ionized impurity scattering and interface roughness scattering (described by a Gaussian correlation function with an average root-mean-square step height of 0.12 nm and an in-plain correlation length of 10 nm).

For our design, the periods are separated by the thickest barrier, i.e., the extraction barrier, as shown in Fig. 1. Only three bound subbands in each period were considered and the effects of continuum states were neglected. Based on the sequential resonant tunneling model [28], the current is the sum of the tunneling current between neighboring periods, I_{ij} ($i = 1 - 3$, $j = 1'' - 3''$). The calculated and measured *I-V* curves are compared in Fig. 4. Stimulated emission was included self-consistently for the calculation of the *I-V* curve. A voltage drop of 2.5 V due to the Schottky barrier and a series contact resistance of 0.3 Ω were used to calibrate the measured *I-V* curve. The calculation shows a good agreement with experimental results, especially for the two current peaks at applied electric fields of 4.8 kV/cm and 15.7 kV/cm. Our DM approach therefore allows the reliable analysis of parasitic current paths. The calculated gain is also shown in Fig. 4. Its peak occurs at 20.5 kV/cm, which agrees well with the measured peak in THz power at 20.2 kV/cm. The calculated threshold bias is 17.7 kV/cm, when an estimated loss of 18 cm^{-1} is included for the gold-gold waveguide structure. This threshold bias is a little smaller than the measured 18.7 kV/cm, indicating a small overestimation of the peak gain. The
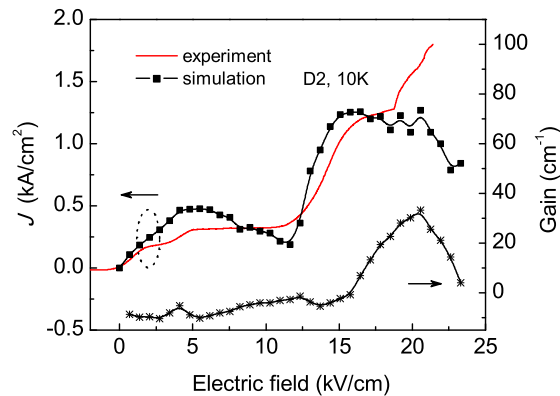
Fig. 4. Comparison of the calculated and measured *I-V* curves (indicated by a dotted ellipse), and the calculated gain as a function of the electric field, of design D2 at 10 K.
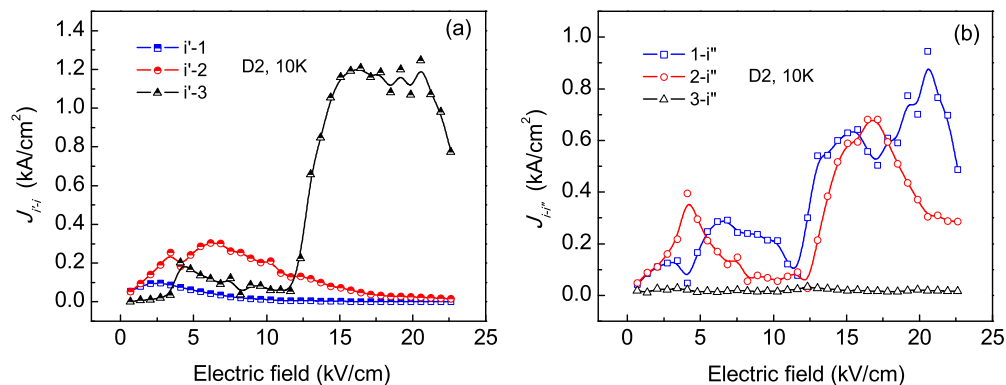

Fig. 5. Calculated resonant tunneling current between neighboring periods of design D2 at 10 K. (a) Total injection current contribution from the upstream period to different subbands 1, 2, and 3. i′ indicates subbands 1′, 2′ and 3′ in the upstream period. (b) Total extraction current contribution from different subband levels to the downstream period. i″ indicates subbands 1″, 2″ and 3″ in the downstream period.

disagreement of *I-V* curves at very high electric fields may be due to neglecting the current through higher energy states and continuum states [25, 29].

The current between neighboring periods was analyzed in order to identify the parasitic paths. The injection current from the upstream period is shown in Fig. 5(a) and the extraction current to the downstream period is shown in Fig. 5(b). On the injection side, the relative contribution of each subband to the total current changes dramatically at an electric field of 12 kV/cm. At lower fields, the current from the upstream period is mainly injected into level 2, and at higher fields, the current to level 3 increases rapidly and becomes the dominant contribution. On the extraction side, the current to the downstream period mostly originates from levels 1 and 2, while the contribution from level 3 is quite small. The current injected into level 3 flows to levels 2 and 1 through the assistance of intraperiod scattering processes. Since the resonant tunneling between different neighboring periods are identical, the current paths can be identified by comparing Figs. 5(a) and 5(b). When the electric field is lower than 12 kV/cm, the carriers are injected from levels 1′ and 2′ to levels 2 and 1, and subsequently a fraction of the carriers in level 2 are scattered to level 1. Finally, the carriers in levels 1 and 2 are extracted to levels 2″ and 1″.
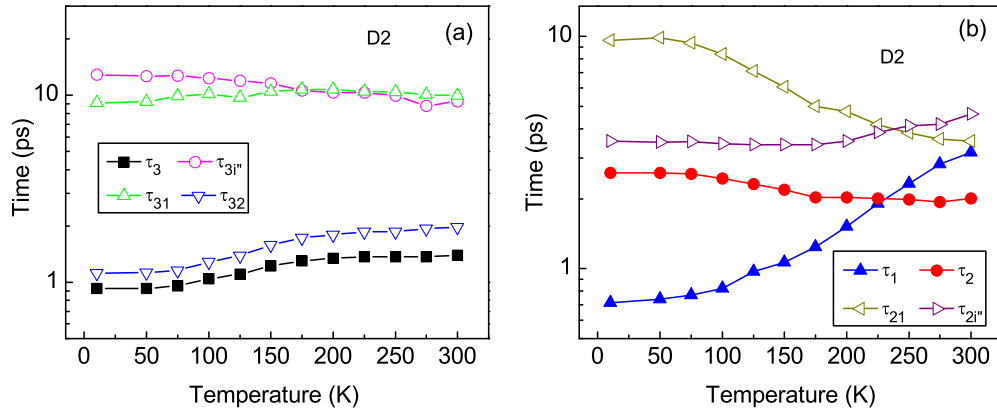
Fig. 6. Temperature evolution of subband lifetime and the key carrier transport time for design D2. (a) The lifetime of subband 3 and the carrier transport time from level 3 to the lower subbands. (b) The lifetime of subbands 2 and 1, and the carrier transport time from level 2 to the lower subbands. i″ indicates subbands 1″, 2″ and 3″ in the downstream period.

The first parasitic current path at a bias of 4.8 kV/cm is mainly from levels 1′ →2→1→ 2″, where level 1 is aligned with level 2″. When the electric field is higher than 12 kV/cm, levels 2 and 1 start to align with level 3″. The carriers are then injected from levels 1′ and 2′ to level 3, relax to levels 2 and 1, and finally are extracted to level 3″. The second parasitic current path is therefore from level 2′ →3→2→ 3″ and 1′ →3→1→ 3″, where the first path is dominant since the scattering rate from level 3 to 2 is much larger than that from level 3 to 1 (shown in Fig. 6). The parasitic current along path 2′ →3→2→ 3″ contributes more than half of the total current at an electric field of 16.8 kV/cm, and 24% at the designed field of 20.5 kV/cm.

Figure 6 shows the temperature dependence of the lifetime of each subband and also the related carrier transport time for design D2 at the design bias. Electrons in level 3 can transport downstream to the next period by resonant tunneling, and to levels 2 and 1 by LO phonon scattering. As shown in Fig. 6(a), the resonant tunneling time to the next period ($\tau_{3i''}$) and the scattering time to level 1 (τ_{31}) are both ~10 ps, which is much longer than the scattering time to level 2 (τ_{32}), which is 1.1 ps. The strong LO phonon scattering between levels 3 and 2 dominates the carrier transport from level 3, and hence leads to the short lifetime of level 3, $\tau_3 = 0.93$ ps at 10 K. Since the current from the upstream period is injected mainly to level 3 (see Fig. 5), the short scattering time τ_{32} gives a high carrier injection efficiency of 83%. For subband 2, as shown in Fig. 6(b), the resonant tunneling time ($\tau_{2i''}$) is much shorter than the scattering time (τ_{21}) at 10 K, which reduces the lifetime of the subband level to $\tau_2 = 2.6$ ps. This short tunneling time $\tau_{2i''}$ is the reason for the large parasitic current from level 2 to 3″. The lifetime of subband 1 is determined by fast resonant tunneling to level 3″ of the downstream period. The short lifetime of level 1, $\tau_1 = 0.70$ ps, results in population inversion between levels 2 and 1. With increasing temperature, τ_1 becomes longer due to dephasing effects; τ_2 is further lowered by the scattering processes, τ_{21}; and τ_{32} increases a little due to LO phonon absorption. The rapid increase in the lifetime of the lower laser level, τ_1, from 0.7 ps to 3.1 ps suggests that the decrease of extraction strength becomes the most important mechanism for the temperature degradation of the device performance. In a similar resonant phonon design [30], the injection time and extraction time are 0.7 ps and 0.3 ps respectively, suggesting further optimization of the extractor is possible for our designs. Thermally-activated LO phonon scattering seems to have less effect on the population loss of the upper laser level, since strong resonant tunneling $\tau_{2i''}$ is the main transport mechanism
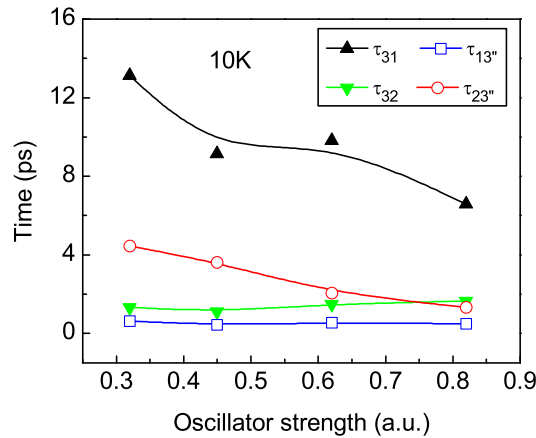
Fig. 7. Calculated carrier transport time of the key relaxation processes from subbands 3, 2 and 1 at the design biases for each versus the scaled oscillator strength.

for the carriers up to 237 K. The small increase of τ_{32} from 1.1 ps to 2.0 ps indicates the reduction of injection efficiency has less effect on the temperature performance.

To better understand the effects of the scaled oscillator strength f_{21}, the calculated carrier transport time at the design bias is shown in Fig. 7. In our design, the barrier separating the two active wells is thinned in order to increase f_{21}. However, thinning this barrier also increases the coupling of the levels $3 - 1$ as well as the coupling of $2 - 3''$, which can be indicated by the decrease of τ_{31} and $\tau_{23''}$. With the increase of f_{21}, the stronger coupling of the levels $3 - 1$ and $2-3''$ results in more carriers transporting through these paths. Note that $\tau_{23''}$ is much smaller than τ_{31}, which means the coupling of the levels 2-3'' dominates these parasitic paths for all four designs. This suggests that suppression of this strong parasitic coupling could result in better device performance, such as smaller current density and higher operating temperatures.

The optical gain ($g \propto \Delta n_{21} f_{21}$, where Δn_{21} is the population inversion) has a complex dependency on the diagonality of the optical transition. To estimate the device performance, the peak gain of the four designs was calculated and the results are shown in Fig. 8. At low temperature (10 K), LO phonon scattering between the laser levels is weak and an increase in f_{21} only results in a small decrease in Δn_{21}. The gain therefore increases from 22.1 cm^{-1} to 43.6 cm^{-1} as f_{21} varies from 0.32 to 0.82. At elevated temperatures, however, thermally activated LO-phonon scattering becomes stronger, leading to a loss of population inversion. In this case, the thermal degradation becomes more significant with increasing f_{21} because of the enhanced LO phonon scattering between laser levels, and the maximum gain will consequently be obtained at an optimum value of f_{21}. The estimated maximum operating temperatures (T_{max}) for designs D1 to D4 are 108 K, 137 K, 151 K and 153 K, respectively. The measured T_{max} are 103 K, 123 K, 113 K and 80 K, respectively, as shown in the inset of Fig. 3(a). The agreement for designs D1 and D2 is better than that for D3 and D4, and the difference between the calculated and measured T_{max} becomes larger with increasing f_{21}. A number of factors, which are not included in our model, may contribute to this discrepancy, and will be discussed next.

5. Discussion

In order to better understand the device performance, several factors arising from our model need to be considered: (1) Continuum states and higher energy states; (2) Interface roughness; and (3) Joule heating. Firstly, our devices are designed to operate at high voltages, and the *I-V* curves at 10 K don't exhibit an obvious NDR behavior after the designed bias (see Fig. 3). At the same time,
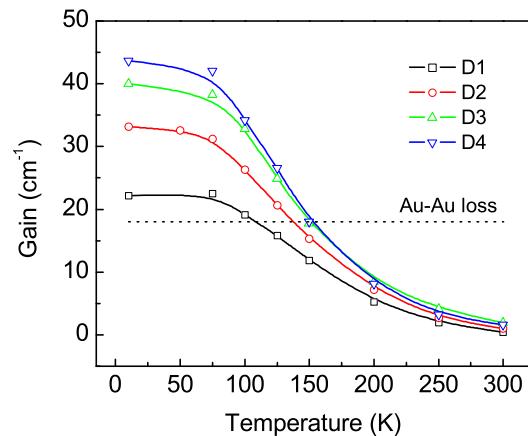
Fig. 8. Calculated peak gain of the four designs as a function of the lattice temperature. The dotted line is the estimated loss of QCLs with gold-gold waveguide configurations.

there is a discrepancy between calculated and measured *I-V* curves in the high voltage range. This indicates that continuum states or higher energy states may assist carrier transport from bound states. Recently, thermally activated leakage into the continuum was found to be an important limiting factor for the temperature performance [25, 26]. This mechanism may contribute to the rapid rapid degradation of the performance of our designs with increasing temperature. As such, including this mechanism in the simulations may help to reduce the discrepancy between the measured and calculated maximum lasing temperatures, and also explain the sensitivity of the maximum lasing temperature to the oscillator strength [31]. Secondly, interface roughness scattering is particularly important in our design since our structures have thin quantum wells, leading to an increase in the number of interfaces. The distribution of interface roughness was found relevant for THz QCLs [32], and therefore an improved description of interface roughness in our model may help to better estimate the device performance. Thirdly, our devices operate with high currents, which may lead to much higher active region temperatures and electron temperatures through Joule heating. This is another possible reason for reduced performance, especially for the designs D3 and D4.

For further improvement of our structures, the parasitic current needs to be suppressed in the initial stages of alignment. In this respect, a thicker extraction barrier or an additional extractor well could be beneficial to weakening the coupling between the upper laser level and extractor level. Application of higher barriers is another option, which could also help to reduce the carrier leakage into the continuum.

6. Conclusion

We have presented experimental and numerical results for a set of extraction-controlled THz QCLs with different radiative diagonality, in which the carrier injection and extraction are achieved by using a single diagonal carrier-phonon scattering process. Such simple structures are ideal for the investigation of scattering injection mechanisms. Based on our model, the parasitic path through the upper laser level to the extractor level was found to relate to the large threshold current density observed in our structures, which could be reduced by optimizing the extraction coupling, leading to higher-temperature operation. We propose that the numerical techniques developed in this work are widely applicable, and may be used for the analysis of parasitic pathways, and subsequent performance optimisation of a wide range of QCL designs.